# Regulating electric double layer in non-fluorinated ether electrolyte enables high-voltage and low-temperature lithium metal batteries

*Renfei Zhao,[1] Yuanhang Gao,[1] Zuosu Qin,[1] Yuelin Li,[1] Tao Zhang,[1] Anqiang Pan,[1] Ning Zhang,[1] Renzhi Ma,[2] Xiaohe Liu[1] and Gen Chen[1]**

[1] School of Materials Science and Engineering, Key Laboratory of Electronic Packaging and Advanced Functional Materials of Hunan Province, Central South University, Changsha 410083, P. R. China

[2] International Center for Materials Nanoarchitectonics (WPI-MANA), National Institute for Materials Science (NIMS), Namiki 1-1, Tsukuba, Ibaraki 305-0044, Japan

Correspondence: geenchen@csu.edu.cn (G. C.)

**Abstract:** The poor oxidation stability of ether-based solvents has long been a major challenge limiting their practical application. To enhance the oxidative stability of ether-based electrolytes, the physicochemical properties of various glycol dimethyl ethers are screened, and diglyme (G2) is selected as the sole solvent for the electrolyte. Lithium bis(fluorosulfonyl)imide (LiFSI), a highly dissociative salt, is used as the primary salt, while lithium nitrate ($LiNO_3$) and lithium difluorophosphate (LiDFP), which have small ionic sizes and strong binding energies, are added as secondary salts. The resulting electrolyte can modulate the electric double layer (EDL) structure by $NO_3^-$ and $DFP^-$ on the cathode side, leading to an increased $Li^+$ concentration that is originally repelled by the cathode. Additionally, the oxidation stability of the electrolyte is improved and the formed electrode-electrolyte interphase (EEI) is more uniform and stable, thereby enhancing the electrochemical performance of the cells. As a result, cells assembled with a total of 1M ternary lithium salt electrolyte in G2 solvent can operate at high voltage of 4.4 V. The Li||NCM811 cells maintain 80.2% capacity retention after 270 cycles at room temperature, with an average Coulombic efficiency of 99.5%, and exhibit 88.4% capacity retention after 200 cycles at −30 °C.

**Keywords:** Lithium metal battery; Ether electrolyte; Electric double layer; High voltage; Low-temperature

## 1. Introduction

In recent years, lithium metal batteries (LMBs) have attracted significant attention as one of the most promising candidates for next-generation energy storage systems, particularly for electric vehicles (EVs) and large-scale energy storage applications [1-3]. Compared to traditional lithium-ion batteries (LIBs), the main advantage of LMBs lies in the use of a lithium metal anode, which enables higher energy density due to ultra-high theoretical capacity (3860 mAh $g^{-1}$) and low electrochemical potential (−3.04 V relative to the standard hydrogen electrode) [4,5]. However, the commercialization of lithium metal batteries still faces several technological challenges [6]. One of the most critical issues is the safety concern. During the charging process, lithium metal may deposit unevenly on the anode surface, resulting in the growth of lithium dendrites [7]. The growth of these dendrites not only results in capacity degradation but can also cause short circuits, overheating, and even thermal runaway, potentially leading to fire or explosion [8,9]. Therefore, the selection and design of the electrolyte for lithium metal batteries are crucial to addressing these issues [10].

Carbonate-based electrolytes are widely utilized in lithium-ion batteries (LIBs) and are the most prevalent electrolyte type in commercial applications [11]. However, carbonate electrolytes suffer from poor reduction stability and limited compatibility with lithium metal anodes [12]. Upon cycling, these electrolytes continuously decompose on the lithium metal anode surface, producing side products and promoting the growth of lithium dendrites [13]. This not only leads to capacity degradation but also significantly impairs Coulombic efficiency (CE) and overall cell capacity retention [14,15]. Moreover, at low temperature, carbonate-based electrolytes exhibit high viscosity and low ionic conductivity, which restricts the performance of the entire cell under cold conditions [16]. In contrast, ether-based electrolytes offer superior reduction stability and better compatibility with lithium metal anodes, resulting in high CE [17]. Additionally, compared to carbonate electrolytes, ether electrolytes have lower viscosity and higher ionic conductivity, leading to enhanced low-temperature performance [18]. However, the oxidative stability of ether-based electrolytes is relatively poor (typically $< 4.0$ V vs. $Li/Li^+$), and they undergo severe decomposition at high voltages at the cathode, generating significant amounts of side products that adversely affect battery performance [19,20].

To address the challenges associated with ether-based electrolytes, two strategies are widely used. The first way is increasing the salt concentration [21]. In high-concentration ether electrolytes, a larger number of $Li^+$ can coordinate with the solvent, which reduces the proportion of free solvent molecules, thereby decreasing the occurrence of side reactions at the cathode. Nevertheless, high-concentration electrolyte exhibits increased viscosity, reduced ionic conductivity, poor wettability, and high costs. To overcome these limitations, researchers have developed locally high-concentration electrolytes by adding co-solvents (such as hydrofluoroether (HFE)) to reduce viscosity [22]. However, most co-solvents remain expensive and pose significant safety concerns during manufacturing, limiting their practical applicability. The second strategy involves introducing fluorine atoms into ether-based solvents to enhance their oxidative stability. However, fluorinated solvents are prohibitively expensive and involve complex processing, further hindering their practical use [23].

In this study, we propose a method for regulating the EDL on the cathode side using lithium salts with small ionic sizes and high binding energies, achieving excellent oxidative stability and electrochemical performance for non-fluorinated ether-based electrolytes at a conventional concentration (1 M). Specifically, Lithium bis(fluorosulfonyl)imide (LiFSI) has a high dissociation degree, which significantly enhances the ionic conductivity of the electrolyte. Lithium nitrate ($LiNO_3$) and lithium difluorophosphate (LiDFP), both having small ionic sizes and high binding energies, exhibit faster voltage response and stronger attraction to $Li^+$ compared to the larger ionic size and weaker binding energy of LiFSI [24]. Molecular dynamics (MD) combined with *in situ* Raman spectroscopy simulations reveal that incorporating 0.6 M LiFSI, 0.2 M $LiNO_3$, and 0.2 M LiDFP into diglyme (G2) can regulate the EDL at the cathode and make oxidation stability of electrolyte stronger. As a result, the Li||NCM811 cells demonstrates excellent electrochemical performance, retaining 80.2% of its capacity after 270 cycles at room temperature with a 1 C charge-discharge rate and 4.4 V cutoff voltage, with an average CE of 99.5%. Even under the extreme condition of −30 °C, Li||NCM811 cells maintain 88.4% capacity retention after 200 cycles at the cutoff voltage of 4.4 V and Li||Cu cells exhibit the CE of 98.8%.

## 2. Results and discussion

### 2.1 Electrolyte composition design

In terms of lithium salts selection, LiFSI was chosen as the primary salt, with $LiNO_3$ and LiDFP used as secondary salts, maintaining a total concentration of 1 molar. LiFSI, while providing high ionic conductivity, can corrode the aluminum (Al) current collector on the cathode side. $LiNO_3$ and LiDFP, although having low solubility in carbonate-based solvents, can dissolve in ether-based solvents, which not only helps the formation of a uniform and stable EEI but also allows for the regulation of the EDL structure on the cathode side [25]. The strong attraction of $NO_3^-$ and $DFP^-$ to $Li^+$ increases $Li^+$ concentration in the cathode-side EDL, promoting their coordination with the solvent, reducing the amount of free solvent, and making oxidation stability of electrolyte stronger. Additionally, LiDFP can improve the battery's low-temperature performance and passivate the Al current collector, mitigating the corrosion effect of LiFSI [26]. To optimize the solvent, we compared the physicochemical properties of several glycol dimethyl ethers: DME (dimethyl ether), G2 (diglyme), G3 (triglyme), and G4 (tetraethylene glycol dimethyl ether). According to density functional theory (DFT) calculations shown in **Figure 1a**, the highest occupied molecular orbitals (HOMO) of G2, G3, and G4 are nearly identical and significantly lower than that of DME, indicating that DME has poorer oxidation stability compared to G2, G3, and G4. However, in terms of the lowest unoccupied molecular orbitals (LUMO), the order is DME > G2 > G3 > G4, suggesting that DME exhibits better reduction stability and is more compatible with the lithium metal anode. Additionally, according to **Table S1**, the density, freezing point, and viscosity of DME and G2 are much lower than those of G3 and G4. Considering the overall physicochemical properties of the solvents, G2 demonstrates excellent oxidative and reduction stability, while its suitable viscosity and freezing point also meet the requirements for low-temperature applications. Therefore, we selected an electrolyte system consisting of LiFSI, $LiNO_3$, and LiDFP as the lithium salts, with G2 as the solvent. This innovative formulation balances multiple advantages and functionalities, with components working synergistically to complement each other, enabling the electrolyte to deliver better performance and adapt to more complex application scenarios. The total concentration of the electrolyte was fixed at a conventional 1 M, and the following compositions were prepared: 0.6 M LiFSI, 0.2 M $LiNO_3$, and 0.2 M LiDFP (denoted as 622); 0.6 M LiFSI and 0.4 M $LiNO_3$ (denoted as 64N); 0.6 M LiFSI and 0.4 M LiDFP (denoted as 64P); and 1 M LiFSI (denoted as 1F) dissolved in G2 solvent.

Through DFT calculations, a screening and analysis of HOMO and LUMO of different lithium salts and solvent molecules was performed (**Figure 1a**) [27]. It was observed that the HOMO energy level of LiFSI is much lower than that of G2. In contrast, the HOMO levels of $LiNO_3$ and LiDFP are significantly higher than that of G2, indicating that these two salts are preferentially oxidized and decomposed at high potentials, which helps to reduce the decomposition of the G2 solvent. The LUMO of G2 is significantly

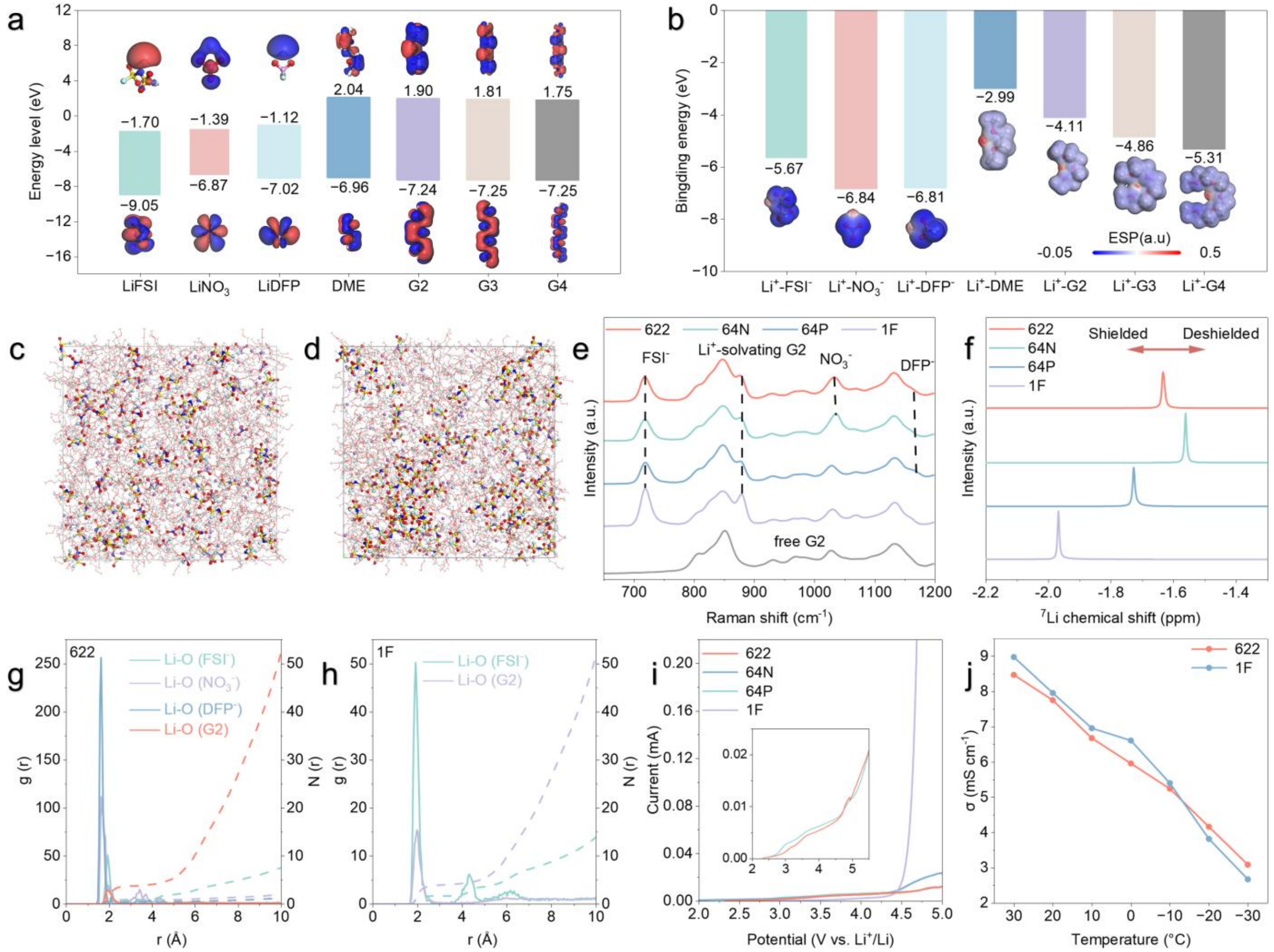

**Figure 1.** Theoretical calculations and experimental characterizations of different electrolytes. (a) Calculated HOMO and LUMO of the solvents and Li salts. (b) The binding energy and electrostatic potential of the $Li^+$-solvent/anion complex. The snapshot of MD simulation trajectories, radial distribution functions and coordination numbers in (c, g) 622 and (d, h) 1F electrolytes. (e) Raman spectra and (f) $^7Li$ NMR spectra of different electrolytes. (i) LSV results of the Li||Al cells at a scan rate of 1 mV $s^{-1}$ in different electrolytes. (j) Temperature dependent conductivities of different electrolytes, ranging from −30 to 30 °C.

higher than the LUMO of the three lithium salts, reflecting the inherent reduction stability of ether solvents and their good compatibility with lithium metal. Additionally, the binding energies between $Li^+$, different anions, and solvent molecules were calculated using DFT. From **Figure 1b**, it is evident that as the chain length of glycol dimethyl ether increases, the binding energy between the solvent and $Li^+$ also increases [28]. The higher binding energies of G3 and G4 result in higher desolvation energies, which is detrimental to battery stability. This is one of the reasons why these two molecules were not chosen as solvents. Furthermore, from the perspective of improving oxidative stability of electrolytes, the electric double layer (EDL) near cathode side is very important. This is because the decomposition of ether solvent molecules primarily occurs near the cathode side. Compared to the widely applied solvation structure model in conventional electrolytes, using the EDL model to explain this process is more reasonable and closer to real-world scenarios. Classical theory posits that the constituents of the first solvation shell are capable of entering EDL and are prone to preferential redox decomposition [29]. However, in the EDL region at the cathode/anode interface, the spatial distribution of solute and solvent, as well as the electronic density, is highly non-uniform, differing significantly from the bulk electrolyte. Under normal conditions, $Li^+$ is repelled from the cathode surface due to electrostatic repulsion, leading to an increase in free solvent molecules near the cathode. This exacerbates the decomposition of the solvent. However, the introduced anions, $NO_3^-$ and $DFP^-$, are small in size, have faster voltage response, and exhibit very high binding energy with $Li^+$. As the voltage on the cathode side increases, the attraction to the anions becomes stronger, causing the anions to move closer to the cathode surface. Due to their strong binding energy, the anions attract the $Li^+$, which would otherwise be repelled, thereby increasing the concentration of $Li^+$ near the cathode. This allows the solvent molecules to coordinate with $Li^+$, reducing the availability of free solvent molecules and mitigating the decomposition of ether solvents at high voltage.

Molecular dynamics (MD) simulations were conducted on the 622 (**Figure 1c, g**) and 1F (**Figure 1d, h**) electrolytes. From **Figure 1g** and **1h**, it is evident that the radial distribution functions (RDF, g(r)) for Li−O($NO_3^-$) and Li−O($DFP^-$) are 1.625 Å and 1.65 Å, respectively, which are significantly smaller than the RDFs for Li−O($FSI^-$) and Li−O(G2) (around 1.925 Å and 1.975 Å). This indicates that $NO_3^-$ and $DFP^-$ anions are more deeply involved in the inner solvation structure and are more likely to coordinate with $Li^+$ compared to the G2 solvent molecules. On the other hand, $FSI^-$ may be involved in the outer solvation shell. However, the coordination number, N(r), of G2 with $Li^+$ is much greater than that of the three anions (**Figure 1g**, **h**), suggesting that $NO_3^-$ and $DFP^-$ actively get involved in the solvation structure, while the primary solvation shell in the bulk electrolyte is primarily composed of solvent molecules, which is largely due to the relatively low concentration of lithium salts. Furthermore, various characterization techniques were employed to further investigate the properties of the bulk electrolyte. **Figure 1e** presents the Raman spectra for different electrolytes. It is evident that compared to 1F, the $Li^+$-solvating G2 peak (around 879.4 $cm^{-1}$) in the 622, 64N, and 64P electrolytes is lower, indicating that in these electrolyte systems, the interaction between $Li^+$ and $NO_3^-$ and $DFP^-$ is stronger, leading to their involvement in the inner solvation structure [30]. The $^7Li$ nuclear magnetic resonance (NMR) spectra in **Figure 1f** shows that the addition of $LiNO_3$ and LiDFP causes the lithium peak to shift to a lower field with higher chemical shift values, indicating stronger interactions between $NO_3^-$ and $DFP^-$ and $Li^+$ compared to G2 solvent molecules [31]. To evaluate the electrochemical stability window of the electrolytes, linear sweep voltammetry (LSV) measurements were conducted with aluminum foil serving as the working electrode. The LSV tests were conducted at a scan rate of 0.5 mV $s^{-1}$. As shown in **Figure S1**, it is apparent that the antioxidative stability of ether-based solvents follows the trend: DME < G2 < G3 < G4. Specifically, DME begins to undergo severe oxidative decomposition at around 4.02 V, which is consistent with the results reported in most ether-based electrolytes at conventional salt concentrations (~1–1.5 M) [16]. G2 and G3 start to show significant oxidation and decomposition around 4.3 V, which marks a considerable improvement in oxidative stability compared to DME. Although G4 exhibits oxidative stability above 4.83 V, its high viscosity, freezing point, and high binding energy with $Li^+$, as previously mentioned, limit its practical performance in batteries, making it unsuitable as a single solvent for electrolyte systems. This will be further discussed in terms of electrochemical performance in later sections. From **Figure 1i**, it is evident that the oxidative stability of the 1F electrolyte is the lowest. The LSV curves for 622 and 64P are nearly identical and are very stable at voltages ≤ 4.5 V. These curves are also more stable than those of 64N, indicating that LiDFP contributes more significantly to improving the oxidative stability of the electrolyte compared to $LiNO_3$. From the perspective of oxidative stability, the 622 and 64P electrolytes exhibit superior performance. In addition to oxidative stability, the viscosity of the electrolyte is also crucial, as it directly affects the electrolyte's impedance and ionic conductivity. As shown in **Figure S2**, from the impedance perspective, the trend is DME < G2 < G3 < G4. To further evaluate the feasibility of the designed electrolyte system for low-temperature battery operation, the ionic conductivity of the 622 and 1F electrolytes were tested at temperatures ranging from 30 °C to −30 °C (**Figure 1j**). The 1F electrolyte exhibited superior ionic conductivity in the moderate temperature range (30 °C to −13 °C), suggesting enhanced ion mobility under these conditions. However, a notable transition occurred below −13°C, where the 622 electrolyte demonstrated better performance, maintaining higher conductivity throughout the lower temperature range (−13 °C to −30 °C). This may be because the composition of the three salts in the 622 electrolyte increases its complexity, which enhances ionic conductivity at low temperatures, thus laying a foundation for its application in low-temperature cells.

### 2.2 Electric double layer

The EDL at the cathode/anode surface plays a critical role during electrochemical reactions. To investigate the interfacial evolution of electrolyte components under operational conditions, in situ Raman spectroscopy was employed to track real-time compositional variations at the cathode-electrolyte interface across different applied potentials, specifically comparing the 622 and 1F electrolyte formulations (**Figure 2a-e**). Compared to $FSI^-$, the smaller sizes and stronger binding energies of $NO_3^-$ and $DFP^-$ result in more pronounced voltage response effects. As the voltage increased from 2.8 V to 4.4 V, the Raman characteristic peak of $FSI^-$ in both the 622 and 1F electrolytes only showed a slight increase with minimal overall change (**Figure 2d**). In contrast, the intensity of the Raman characteristic peaks for $NO_3^-$ and $DFP^-$ in the 622 electrolyte composition increased significantly with increasing voltage (**Figure 2e**). As the voltage increased, $NO_3^-$ and $DFP^-$ accumulated at the positive electrode side of the 622 system. Due to the high binding energy between $NO_3^-$, $DFP^-$ and $Li^+$, they are able to attract $Li^+$, which would otherwise be repelled by the positive electrode, allowing these $Li^+$ to enter the EDL and form lithium-ion-solvent complexes with free G2 solvent molecules inside the EDL. **Figure S3** further illustrates the trend of Raman characteristic peak changes for free and complexed solvent molecules under different voltage. As the voltage increased, the free G2 in the 622 system continuously decreased, while the G2 complexed with $Li^+$ increased. In contrast, in the 1F electrolyte, free G2 significantly increased while complexed G2 decreased. This is because $NO_3^-$ and $DFP^-$ have stronger electronegativity and a higher binding energy with $Li^+$ than $FSI^-$. In the control group 1F, as the voltage increased, the repulsive effect of the positive electrode on Li$^+$ intensified, resulting in fewer Li$^+$ near the positive electrode that could coordinate with the solvent, and an increased free solvent. However, in 622 electrolyte, the strong binding ability of $NO_3^-$ and DFP$^-$ to Li$^+$ can mitigate the repulsion from the positive electrode, thereby increasing the number of Li$^+$ that can coordinate with free solvent molecules near the positive electrode, which helps reduce solvent

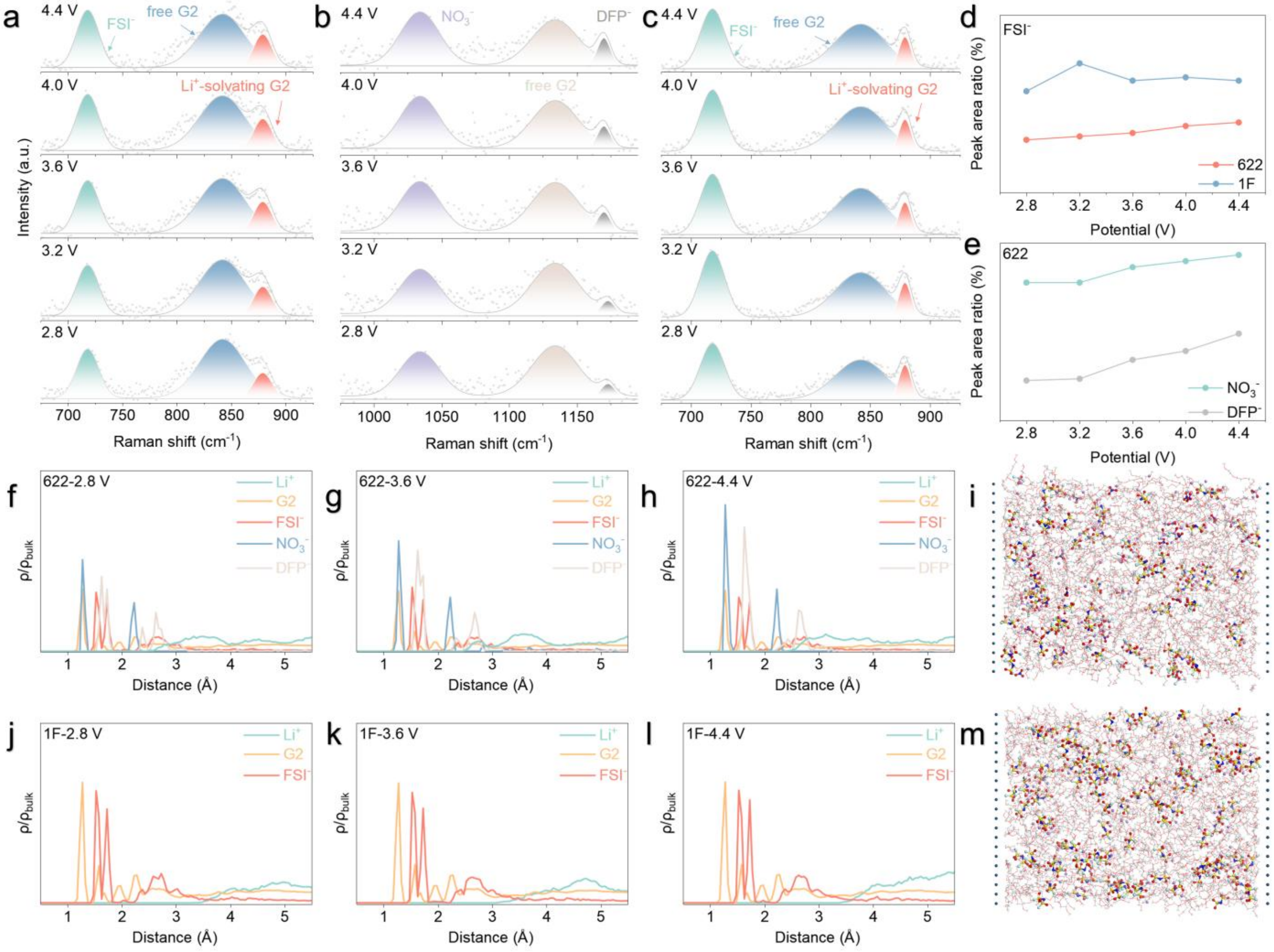

**Figure 2.** In situ Raman spectra of the cathode surface layer under different voltages in (a, b) 622 and (c) 1F. The variation trend of different electrolyte components in *in situ* Raman spectra with (d) FSI$^-$ in 622 and 1F, (e) $NO_3^-$ and DFP$^-$ in 622. Component distribution plots and MD simulation snapshots near to cathode surface in (f-i) 622 and (j-m) 1F at different voltages.

decomposition. To further validate the accuracy of the *in situ* Raman characterization and the voltage response effect of $NO_3^-$ and $DFP^-$ in the positive electrode side of the EDL, molecular dynamics (MD)simulations were performed on the electrolytes at three voltages (2.8 V, 3.6 V, and 4.4 V) by applying a constant potential to the solvent box (**Figure 2i**, **m**). **Figure 2f-h**, and **Figure 2j-l** show the distribution of different components near the positive electrode for the 622 and 1F electrolyte compositions, respectively. As the voltage increased, the number density of $NO_3^-$ and $DFP^-$ in the 622 system increased, which is consistent with the *in situ* Raman results, while the $FSI^-$ density remained relatively stable with no significant changes. The $Li^+$ closest to the positive electrode in the 622 system was located around 2.475 Å, while in the 1F system, the closest $Li^+$ was positioned around 3.375 Å. This further reflects that the lack of $NO_3^-$ and $DFP^-$ in the 1F electrolyte results in an unregulated EDL, where the repulsive effect of the positive electrode causes $Li^+$ to be positioned further away, reducing the coordination of $Li^+$ with solvent molecules within the EDL, and increasing the amount of free solvent, which accelerates solvent decomposition [32]. These simulation results demonstrate the significant voltage response effect of $NO_3^-$ and $DFP^-$, their strong adsorption to $Li^+$, and their ability to increase the concentration of $Li^+$ within the EDL, which is consistent with the in situ Raman experimental findings. In summary, $NO_3^-$ and $DFP^-$ can construct a favorable EDL rich in $Li^+$, where $Li^+$ is well coordinated with solvent molecules. This unique interfacial structure exhibits distinct characteristics compared to the solvent arrangement in the bulk electrolyte, thereby substantially enhancing the electrolyte's oxidative stability.

### 2.3 Electrochemical performance

$LiNi_{0.8}Co_{0.1}Mn_{0.1}O_2$ (NCM811) (9.2 mg cm$^{-2}$, 1 C = 200 mA g$^{-1}$) was selected as the cathode material to conduct electrochemical experiments and characterizations to evaluate the potential application of the electrolyte [33,34]. **Figure 3a** shows the performance of Li||NCM811 cells assembled with electrolytes containing different salts. The cells were tested at room temperature with a 1C charge/discharge rate and a 4.4 V high cutoff voltage. The 622-based cell exhibited an initial CE of 92.1%, with 88.6% capacity retention after 200 cycles, 80.2% retention after 270 cycles, and an average CE of 99.5% after 300 cycles. In contrast, the initial CE for the 64N, 64P, and 1F cells were 78.4%, 88.4%, and 87.2%, respectively. The 64N-based cell, with the lowest initial CE, showed only 58.7% capacity retention after 100 cycles, with an average CE of only 97%. Both 64P and 1F showed relatively better performance than 64N, but after 200 cycles, their capacity retention was only 41.1% and 35.7%, with average CEs of 97.8% and 98.2%, respectively. It is preliminarily hypothesized that LiDFP primarily acts on the high-voltage positive electrode side, forming a stable CEI, while $LiNO_3$ mainly acts on the negative electrode side, forming a good SEI. Furthermore, the synergistic effect of the three salts in increasing entropy may also contribute to improved oxidative stability [35]. As shown in **Figure S4**, the performance of Li||NCM811 cells with different LiFSI concentrations in the electrolyte system was tested, while keeping the concentrations of $LiNO_3$ and LiDFP fixed. It was found that the most reasonable salt combination was 0.6 M LiFSI, 0.2 M $LiNO_3$, and 0.2 M LiDFP. Additionally, Li||NCM811 cells tests with DME, G3, and G4 solvents (**Figure S5**), using the same lithium salt composition as 622, were performed. DME, due to its high HOMO, has poor oxidative stability. Although it showed excellent CE, its capacity retention was unsatisfactory, with only 74.5% capacity retention after 170 cycles. G3 and G4, with higher HOMO, exhibited excellent oxidative stability, but in Li||NCM811 cells tests, they showed a sudden drop in CE. This could be attributed to their low LUMO and poor reduction stability, as well as their higher viscosity, which leads to concentration polarization and greater damage to the battery. LiFSI was replaced with LiTFSI, while all other components remained unchanged, and Li||NCM811 cells were assembled for testing (**Figure S6**).

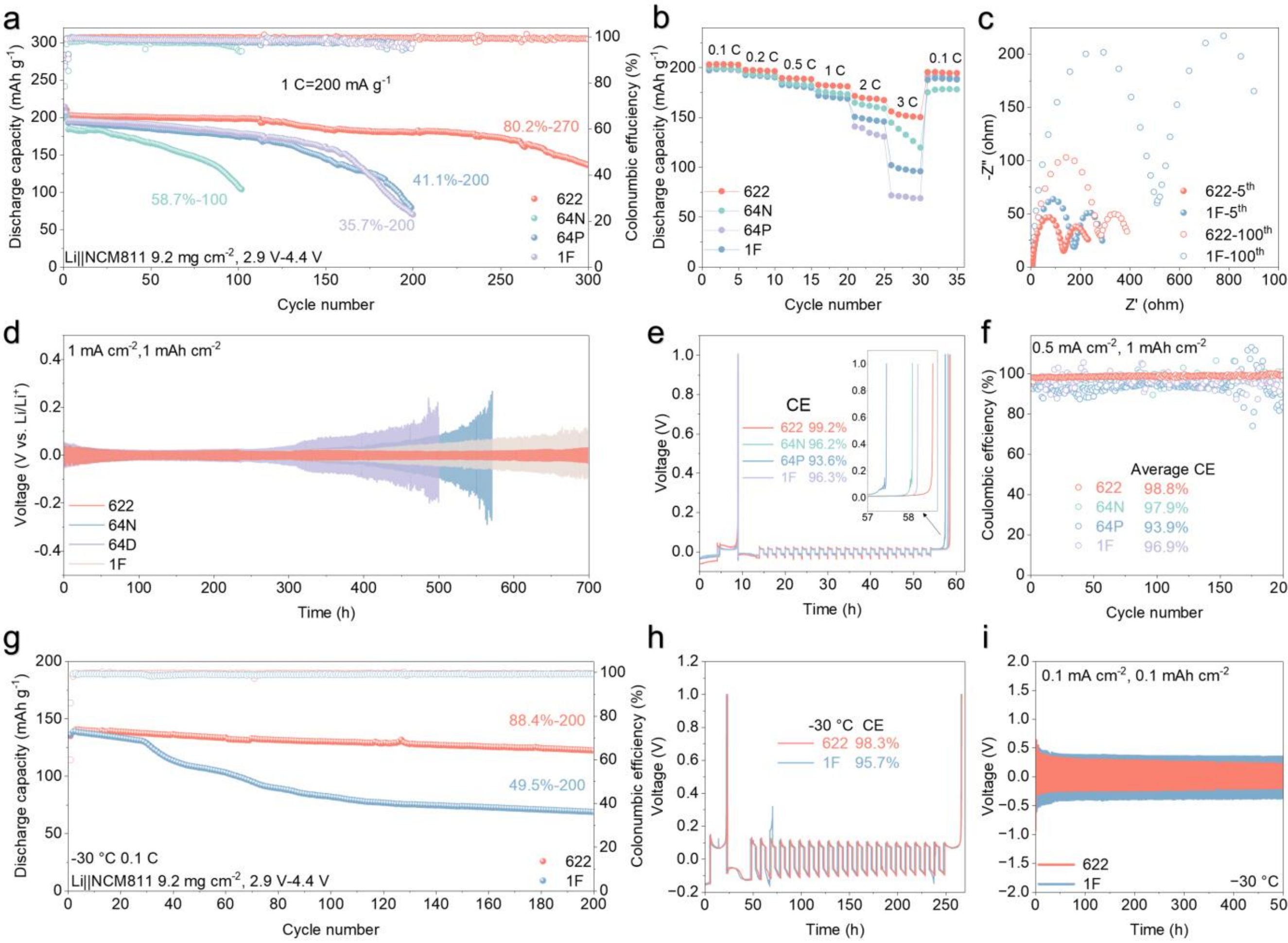

**Figure 3.** Electrochemical performance of different electrolytes. (a) Long-term cycling performance in Li||NCM811 cells at 1 C between 2.9 and 4.4 V. (b) Rate performance in Li||NCM811 cells. (c) Nyquist plots of Li||NCM811 cells at 5th and 100th cycle using different electrolytes. (d) Cycling stability of Li||Li symmetric cells at 1.0 mA cm$^{-2}$ with a fixed capacity of 1.0 mAh cm$^{-2}$. (e, f) Li metal plating/stripping CE evaluated by Li||Cu cells at 0.5 mA cm$^{-2}$ with a fixed discharge capacity of 1.0 mAh cm$^{-2}$. (g) Cycling performance of Li||NCM811 cells with different electrolytes at −30 °C. (h) CE tested by Li||Cu cells of Aurbach method at −30 °C. (i) Cycling stability of Li||Li symmetric cells at 0.1 mA cm$^{-2}$ with a fixed capacity of 0.1 mAh cm$^{-2}$ at −30 °C.

However, the CE and capacity retention were poor, clearly indicating that LiTFSI is not suitable as the main salt. BE (1M $LiPF_6$ in EC/DMC = 1:1 vol%), the most widely used commercial electrolyte, was also tested in a Li||NCM811 cells configuration (**Figure S6**). The BE cell exhibited 70.3% capacity retention and an average CE of 98.87% after 200 cycles, indicating that the 622 electrolyte system demonstrates superior electrochemical performance compared to the commercial electrolyte. In the rate performance test (**Figure 3b**), the 622 Li||NCM811 cell showed a stable discharge capacity of 151.57 mAh $g^{-1}$ at a 3 C high rate, outperforming 64N (132.39 mAh $g^{-1}$), and far exceeding 64P (97.56 mAh $g^{-1}$) and 1F (70.21 mAh $g^{-1}$), reflecting the excellent kinetic performance and fast-charging capability of the 622 system. To further assess the kinetics, we tested the Nyquist plots of the Li||NCM811 cells with different electrolyte compositions for the 5th and 100th cycles (**Figure 3c**, eqxuivalent circuit shown in **Figure S7**). The 622 cell exhibited lower $R_{int}$ and $R_{ct}$ than 1F and maintained lower levels even after long-term cycling, confirming that the 622 electrolyte optimizes the CEI and SEI and significantly enhances interfacial kinetics [36].

In room-temperature Li||Li symmetric cell tests (**Figure 3d**), the 622-based cell exhibited stable and small overpotentials over a long cycling period of 700 hours, with the overpotential after 700 hours being only 29.7 mV. In contrast, the 1F-based cell reached an overpotential of 111.3 mV after 700 hours. Due to the excellent compatibility of ether-based electrolytes with lithium metal anodes, the performance of the four symmetric cells in **Figure 3d** is significantly better than that of BE in terms of stability (**Figure S8** shows the symmetric long-cycle test of BE), with smaller overpotentials. The 64P and 64N cells even performed worse than the 1F cell, suggesting that the addition of $LiNO_3$ and LiDFP has a significant impact on impedance and reaction kinetics. To further study the compatibility of the electrolyte with the lithium metal anode, the reversibility of the lithium plating/stripping process was measured (**Figure 3e** and **3f**). First, CE was tested using the Aurbach method. The 622 cell achieved a CE of 99.2%, which is superior to 1F (96.3%) and 64N (96.2%), and significantly higher than 64P (93.6%). Subsequently, the CE was tested using the traditional Li||Cu cells long-cycle testing method. In a 200-cycle long-cycle test, the 622-based cell demonstrated an average CE of 98.8%, with highly stable CE throughout the cycles and no significant fluctuations. This performance was notably superior to the 64N (97.9%), 64P (93.9%) and 1F (96.9%) cells, which exhibited large fluctuations in CE during cycling, especially the 64P cell. Due to its excellent CE and reversibility, the 622-based Li||NCM811 cell can provide a higher capacity, which also explains why the 622 Li||NCM811 cell provided the highest initial discharge capacity in **Figure 3a**.

To evaluate the low-temperature feasibility of different electrolyte compositions, electrochemical tests were conducted on Li||NCM811 cells, Li||Cu cells, and Li||Li symmetric cells at −30 °C (**Figure**s **3g-i**). First, the Li||NCM811 cell performance was tested at −30 °C with a 0.1C charge/discharge rate and a cutoff voltage of 4.4 V (**Figure 3g**). The 622 cell exhibited an initial discharge capacity of 139.2 mAh $g^{-1}$ and a first-cycle CE of 93.2%. After 150 cycles, it showed a capacity retention of 91.2%, in sharp contrast to the 1F cell, which had a first-cycle CE of only 86% and a capacity retention of only 53.2% after 150 cycles. We also tested the CE of the Li||Cu cells at −30 °C using the Aurbach method (**Figure 3h**). The 622 cell had a CE of 98.3%, while the 1F cell had a CE of only 95.7%. Moreover, the Aurbach voltage curve of the 1F cell was unstable, with abrupt changes occurring between 60-70 hours. Additionally, we tested the Li||Li symmetric cells at −30 °C. While both the 622 and 1F cells showed stable overpotentials for 500 hours, the overpotential of the 1F cell (0.3752V) was significantly higher than that of the 622 cell (0.1964 V) after 500 hours. The EIS of the Li||NCM811 full cells was assessed with electrolyte of group

622 and 1F after 5 and 50 cycles at −30 ° C. From the **Figure S9**, the impedance of group 622 at 5th and 50th cycle remains similar, indicating that group 622 has formed stable SEI and CEI in the first five cycles. However, the EIS at 5th cycle of the 1F group is very large, and the counterpart at 50th cycle is even larger. It can be deduced that the CEI and SEI are continuously thickening and the desolvation energy is high. Moreover, the optical and SEM data (**Figure S10**) of low-temperature lithium deposition show that the deposition of group 622 is relatively uniform and dense, while group 1F is obviously uneven. It is also noteworthy that the copper foil edge is barely covered by lithium metal deposition. SEM images also reflect a large number of dendritic lithium in group 1F. In addition, the electrochemical tests of Li||NCM811 full cells at low temperature −30 °C with different rate were shown in **Figure S11**. Under the rate of 0.1 and 0.2 C, the discharge capacities of groups 622 and 1F are basically the same. However, under the condition of 0.5 C, the difference gradually increases. The specific discharge capacity of group 622 is about 81 mAh $g^{-1}$, higher than group 1F (42 mAh $g^{-1}$). This may be attributed to that the $LiNO_3$ and LiDFP in group 622 are deeply involved in the shell of the inner solvation structure, weakening the coordination structure of the solvent to $Li^+$, thereby reducing the desolvation energy of $Li^+$ and optimizing the rate performance of the battery. Overall, the cells assembled with the 622 electrolyte exhibit excellent electrochemical performance at −30°C, demonstrating the promising potential of the designed electrolyte system under low-temperature conditions.

## 2.4 Characterization of Li metal and NCM811 cathode

To comprehensively analyze the evolution of the CEI and the cathode structure, scanning electron microscopy (SEM) and transmission electron microscopy (TEM) were used to characterize the NCM811 cathode after cycling (**Figure 4a-d**). After 100 cycles at a 1C charge/discharge rate in Li||NCM811 cells, TEM imaging revealed the formation of a thin and compact CEI layer approximately 5-6 nm thick in the 622-based cells (**Figure 4a**). SEM images also showed that the cathode particles of the 622 cell remained intact, with no cracks or structural collapse (**Figure 4b**). In contrast, after 100 cycles, the CEI thickness in the 1F cell was approximately 18-21 nm (**Figure 4c**), three times thicker than the CEI in the 622 cell. Additionally, SEM scans showed significant structural collapse of the cathode particles in the 1F cell, with severe damage to the particle integrity (**Figure 4d**) [37]. X-ray photoelectron spectroscopy (XPS) was used to analyze the chemical composition of the CEI after 100 cycles in Li||NCM811 cells with different electrolyte systems [38]. As shown in the C1s spectra (**Figure 4e**), the C-C/C-H peak in the 622 electrolyte system was significantly lower than that in the 1F system.[7] The top portion of **Figure 4k** more clearly reflects the change in the intensity of the C-C/C-H peak, indicating that the organic content in the CEI layer of the 622-based electrolyte is lower than in the other electrolyte systems, with G2 solvent decomposition being suppressed. In the BE group, the C 1s (**Figure S12a**) spectrum shows higher peaks for C-O and C-C/C-H, and the intensity of the $CO_3^{2-}$ and C=O peaks is much higher than in the four electrolyte systems shown in **Figure 4e**, indicating that solvent decomposition in carbonate-based electrolytes is more severe, resulting in higher organic content in the CEI [39]. The M-O peak in **Figure 4f** represents the bonding between transition metals (Ni, Co, Mn) and oxygen. The M-O bond intensity in the CEI of the 622 group was significantly higher than that in the 1F group (**Figure 4k**, lower part). M-O bonds are typically detectable within the CEI, indicating that the CEI of the 622 system is thinner and denser than that of the 1F system, which is one of the advantages of less solvent decomposition [40]. In contrast, the BE group (**Figure S12b**) did not even have M-O peak, further suggesting a thicker CEI and higher organic content. Additionally, the $Li_3N$ (399.0 eV) and LiF (684.6 eV) peaks in the 622 electrolyte system were significantly higher than in the 1F system (**Figure 4j-l**), indicating that the addition of $LiNO_3$ and LiDFP promotes their preferential decomposition, greatly enhancing the inorganic content of the CEI. $Li_3N$, with its high chemical stability and conductivity, helps form a stable interface layer and regulates electronic conductivity and interface conductivity, while LiF, with high electronic insulation and ionic conductivity, facilitates efficient $Li^+$ conduction between the electrode and electrolyte, thereby improving the overall electrochemical performance of the cells. Furthermore, the CEI in the 622 electrolyte system showed a high P-O bond intensity (**Figure 4i**), which not only reflects the preferential decomposition of LiDFP but also indicates that phosphate groups interact with $Li^+$ to form an interface layer with certain ionic conductivity. Phosphates formed by the interaction between phosphate oxides and lithium salts in the electrolyte help improve the ionic conductivity of the interface layer, enabling more efficient $Li^+$ transport between the electrode and electrolyte. This contributes to improved charging/discharging efficiency and rate performance of the battery. Additionally, the S 2p spectra in **Figure 4j** reveal higher sulfur content in the CEI of the 622 group, which is attributed to the decomposition of $FSI^-$ anions. This indicates that the multi-salt electrolyte system has a synergistic effect, promoting the decomposition of various lithium salts, thereby increasing the inorganic content of the CEI and improving the oxidative stability of the electrolyte. In contrast, the F 1s spectra (**Figure S12c**) and P 2p spectra (**Figure S12d**) in the BE group show higher peaks for C-F and P-F, reflecting severe decomposition of $LiPF_6$. The decomposition products, such as HF, severely affect both the anode and cathode, damaging the battery's performance, which is a major reason for the poor performance of carbonate-based electrolyte Li||NCM811 cells.

To comprehensively analyze the evolution of the SEI and the anode structure, SEM was employed to examine the lithium metal anode. **Figure 5a** and **5c** show the surfaces of the lithium metal anodes in Li||Li symmetric cells assembled with 622 and 1F electrolyte systems after 50 cycles. It can be observed that the surface of the 622 anode is very smooth, while the 1F anode surface exhibits a significant amount of lithium dendrites and is quite rough. **Figure S13** presents cross-sectional SEM images of lithium metal anodes after 50 cycles in Li||Li symmetric cells assembled with 622 (**Figure S13a, b**), 64N (**Figure S13c,**

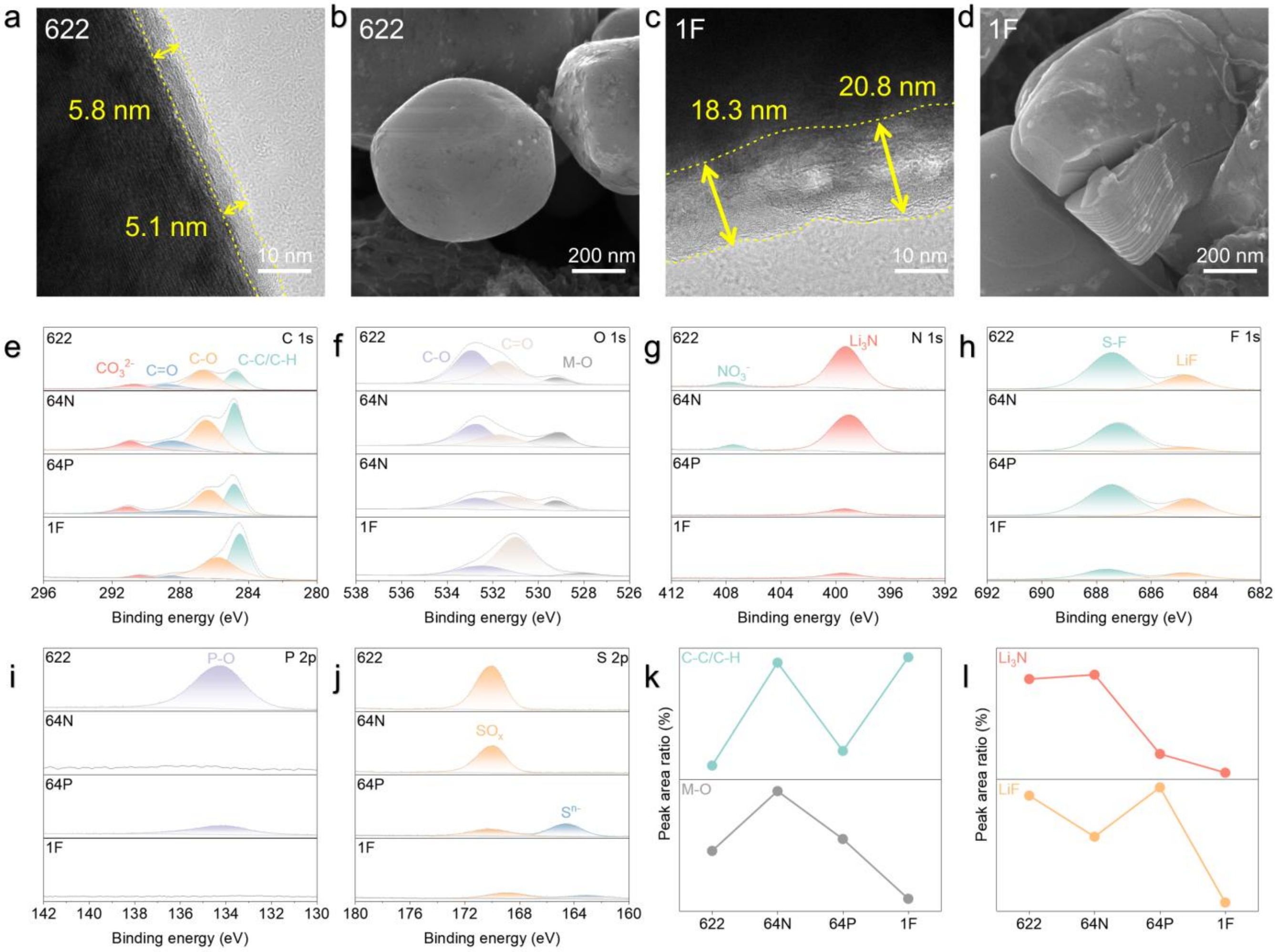

**Figure 4.** TEM and SEM images of NCM811 electrode cycled with (a, b) 622 and (c, d) 1F electrolytes for 100 cycles. (e) C 1s, (f) O 1s, (g) N 1s, (h) F 1s, (i) P 2p and (j) S 2p XPS spectra of NCM811 cathode cycled with different electrolytes after 100 cycles. (k, l) The analysis of CEI composition based on XPS spectra.

**d**), 64P (**Figure S13e, f**), 1F (**Figure S13g, h**), and BE (**Figure S13i, j**) electrolyte systems. The lithium metal anode in the 622 electrolyte system shows the smoothest surface with minimal dendrite formation, far superior to the other systems, especially the BE electrolyte, where the surface is the roughest, with the thickest dendrites and dead lithium. Additionally, we used a current density of 0.5 mA $cm^{-2}$ to deposit 4 mAh $cm^{-2}$ of lithium onto a copper collector. The lithium deposition on the collector in the 622 system is very dense and compact (**Figure 5b**), while the lithium deposited in the 1F system is looser and sparser (**Figure 5d**). Lithium deposition images for other electrolyte components are shown in **Figure S14**. The DME-based electrolyte (**Figure S14c**) shows denser lithium deposition than the G3 (**Figure S14d**) and G4 (**Figure S14e**) electrolyte systems, whereas the BE electrolyte (**Figure S14f**) exhibits dendritic lithium deposition on the collector surface, which is fragmented and broken.

We further conducted X-ray photoelectron spectroscopy (XPS) depth sputtering analysis to investigate the surface composition of the lithium metal anode after 50 cycles in the Li||Li symmetric cells. **Figure 5e** and **5i** present the C 1s sputtering spectra for the 622 and 1F systems. The carbon content on the surface of the lithium metal anode in the 622 system is slightly lower than in the 1F system. However, as the sputtering process thinned the surface, the carbon content in the 622 system decreased significantly, indicating fewer organic components in the internal SEI, while the carbon content in the 1F system did not significantly decrease during the sputtering, confirming that the 622 system inhibits solvent decomposition. In the O 1s spectra (**Figure 5f** and **5j**), the C=O and Li-O peaks in the 622 system are relatively lower, and the intensity of these peaks decreases significantly with sputtering. In contrast, the 1F system exhibits high C=O and Li-O peak intensities, which do not change significantly even after sputtering, suggesting that the 1F system has a larger amount of dendritic lithium and a thicker SEI. The

Li-O bonds likely result from the ether bond decomposition of the G2 solvent reacting with lithium metal, further confirming that the 622 electrolyte inhibits solvent decomposition. Similar to the N 1s and F 1s spectra for the cathode, the 622 system shows higher intensities for $Li_3N$ and LiF, and as sputtering progresses, the $Li_3N$ intensity remains stable (**Figure 5j**), while the LiF intensity even increases significantly (**Figure 5h**), indicating that the SEI in the 622 system is very uniform and stable. The formation of lithium fluoride can suppress lithium dendrite growth by improving the structure of the SEI, and the high interfacial adsorption energy of $Li_3N$ effectively regulates the lithium plating/stripping behavior in the 622 system, improving the electrochemical kinetics. In the S 2p spectra, the $Li_2S$ content in the 622 system (**Figure S15a**) is significantly lower than in the 1F system (**Figure S15c**), further confirming that the $LiNO_3$ and LiDFP additives displace the original inner solvation structure of LiFSI, reducing the decomposition of LiFSI. **Figure S16** presents the sputtering XPS spectra for the BE electrolyte system. The C 1s (**Figure S16a**) and O 1s (**Figure S16b**) spectra are similar to those of the cathode XPS results, showing very high carbon and oxygen content, which remains high even after 180 seconds of sputtering, much higher than the 622 system. This suggests that the BE electrolyte's anode SEI is composed of a thick layer of organic material. While LiF can improve the SEI structure and suppress dendrite growth, the LiF in the BE system does not inhibit dendrite formation, as shown by the SEM images of the BE anode. This is because the LiF in the BE system originates from the decomposition of $LiPF_6$, which is accompanied by the generation of HF and $H_2O$, both of which severely harm the anode [41]. The extremely high P-O peak in the P 2p spectrum of **Figure S16** further corroborates this point, supporting the conclusion that the decomposition of $LiPF_6$ is harmful to the anode and impacts battery performance.

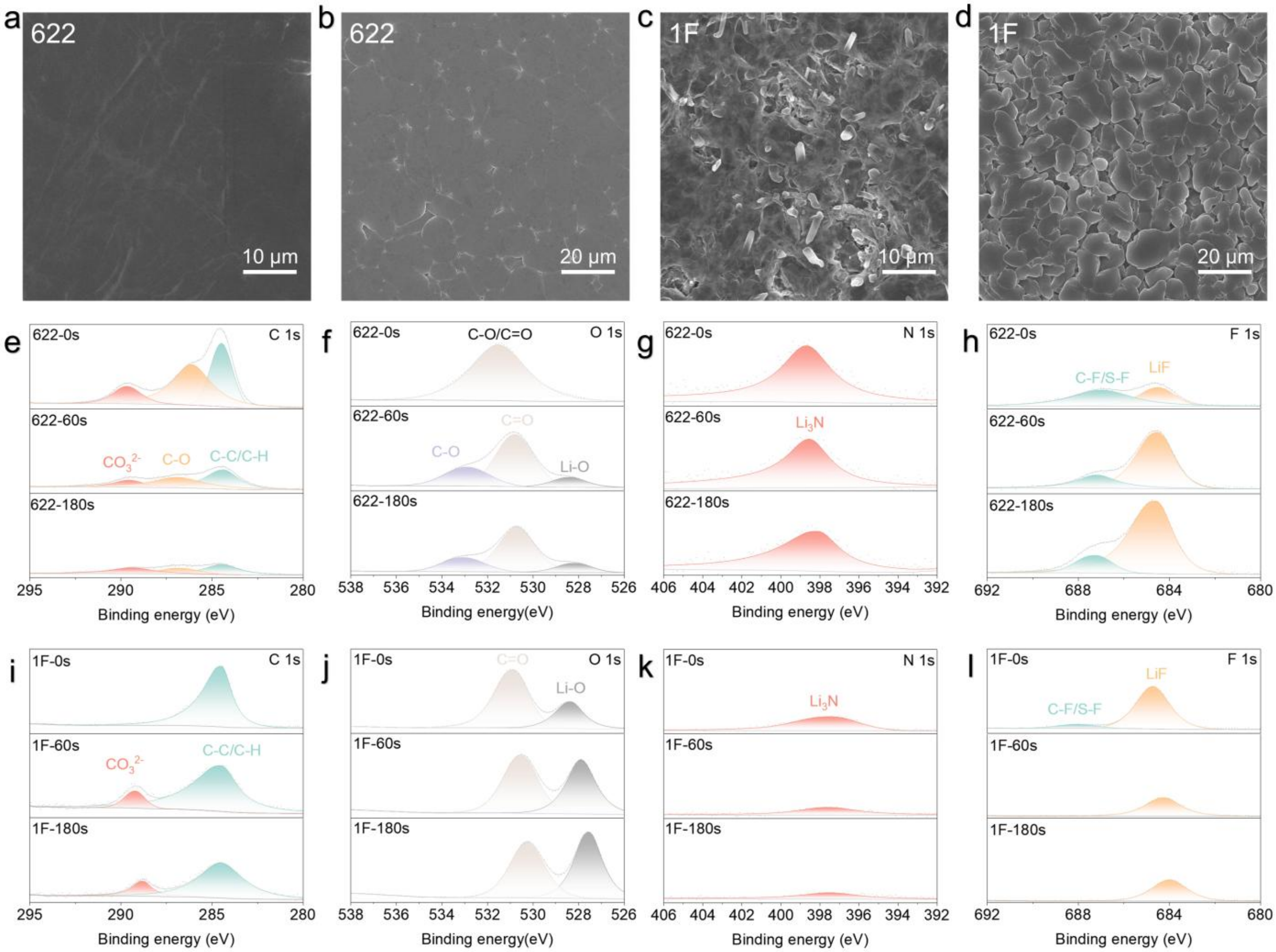

**Figure 5.** SEM analysis of the Li metal recovered from Li||Li symmetric cells after 50 cycles with (a) 622 and (c) 1F electrolytes. SEM images of (b, d) top view of 4.0 mAh $cm^{-2}$ Li deposited on Cu foil at 0.5 mA $cm^{-2}$ in different electrolytes. The comparison of XPS (e, i) C 1s, (f, j) O 1s, (g, k) N 1s and (h, l) F 1s spectra of Li-metal anodes after 50 cycles in Li||Li symmetric cells a with various etching time in different electrolytes.

## 3. Conclusions

In summary, we proposed an electrolyte engineering strategy to regulate the EDL structure on the cathode side using three lithium salts with a total concentration of 1 M, thereby achieving non-fluorinated solvent, low-cost, and excellent high-voltage and low-temperature electrochemical performance. The introduction of two lithium salts with high binding energies and small volume, $LiNO_3$ and LiDFP, completely altered the EDL structure on the cathode side at high cutoff voltages. This modification allowed more $Li^+$ to coordinate with the solvent, thereby reducing the amount of free solvent and enhancing the oxidation stability of the electrolyte. Additionally, the use of the single-solvent G2 effectively overcame the solubility issues of $LiNO_3$ and LiDFP in carbonate-based electrolytes. The designed electrolyte formed a thin, stable CEI and SEI enriched with F and N, improving the electrochemical performance significantly. As a result, Li||NCM811 cells exhibited a capacity retention of 80.2% after 270 cycles at 4.4 V at room temperature, with an average CE of 99.5%. Furthermore, at −30 °C and 4.4 V, the cells maintained 88.4% capacity retention after 200 cycles. This strategy of regulating the EDL structure to stabilize ether-based electrolytes at high voltage provides an environmentally friendly, low-cost, and simple yet effective approach for advanced electrolyte of LMBs.

## 4. Experimental Section

### 4.1 Materials and Electrolytes preparation

Metallic lithium (Li, 99.99%, 0.45 mm thick, 12.5 mm in diameter) was obtained from Zhongneng Technology. 1,2-dimethoxyethane (DME) (99%), Diethylene glycol dimethyl ether (G2) (≥99%), Triethylene glycol dimethyl ether (G3) (≥99%), Tetraethylene glycol dimethyl ether (G4) (≥99%) were obtained from Aladdin Co., Ltd. The baseline electrolyte (BE) composed of 1 M $LiPF_6$ in EC/DMC (1:1 by vol.), Lithium bis(fluorosulfonyl)imide (LiFSI) (≥99.9%), Li difluorophosphate (LiDFP, 99.9%) and Lithium nitrate ($LiNO_3$, 99.9%) was obtained from Dodochem Technology. The $LiNi_{0.8}Co_{0.1}Mn_{0.1}$(NCM811) cathode was provided by Canrd Technology featuring an active material mass loading of 9.2 mg cm$^{-2}$. Before the cell assembly, the NCM811 electrodes underwent vacuum drying at 85 °C for 12 h. All electrolytes and coin cells were prepared in an argon-filled glove box with $O_2 < 0.01$ ppm and $H_2O < 0.01$ ppm. 0.6 M LiFSI, 0.2 M $LiNO_3$, 0.2 M LiDFP or 0.6 M LiFSI and 0.4 M $LiNO_3$ or 0.6 M LiFSI and 0.4 M LiDFP or 1M LiFSI were dissolved into G2, denoted as 622, 64N, 64P and 1F, respectively.

**4.2 Electrochemical measurements**

Electrochemical performance was evaluated using CR2025 coin cells assembled with Celgard PE separators. The lithium plating/stripping Coulombic efficiency (CE) in various electrolyte systems was quantitatively determined through Li||Cu cells employing the Accurate Determination method. Specifically, 2 or 3 fold of Li plating capacity $Q_T$ was pre-deposited at a current density of 0.5 mA cm$^{-2}$. Then a fixed capacity ($Q_C$ =0.5 mAh cm$^{-2}$) of Li metal was stripped/plated for n cycles. Finally, a capacity retention ($Q_R$) was measured by a final Li stripping process at 0.5 mA cm$^{-2}$. The CE value can be calculated by the following equation: CE = (n $Q_C + Q_R$) / (n $Q_C + Q_T$). In addition, the Li plating/stripping CE's stability was tested using Li||Cu cells. The half cells were first activated at 0.05 mA cm$^{-2}$ for five cycles (0 V to 1 V) to stabilize the SEI and remove electrode impurities. Following this activation protocol, the cells were subjected to repeated plating/stripping cycles under controlled conditions: lithium was deposited on the copper current collector with a fixed capacity of 1.0 mAh cm$^{-2}$, followed by stripping to a cut-off voltage of 1.0 V. Li||Li symmetrical cells were cycled at 1.0 mA cm$^{-2}$ or 0.1 mA cm$^{-2}$ for 1.0 h in each half cycle. For Li||NCM811 (active material loading is 9.2 mg cm$^{-2}$ with the areal capacity around 1.84 mAh cm$^{-2}$) cells with electrolyte up to 40−50 μL were tested at 1C (1C = 200 mAh g$^{-1}$) between a voltage range of 2.9−4.4 V. Rate performances were tested at 0.1, 0.2, 0.5, 1, 2, 3 C to evaluate the fast charging/discharging feature.

## 4.3 Characterizations

The morphological characterization of lithium metal was performed using scanning electron microscopy (SEM, MIRA3 TESCAN). Surface chemical analysis was conducted with a high-sensitivity X-ray photoelectron spectrometer (XPS, Thermo Scientific K-Alpha+). Prior to characterization, all electrodes were meticulously rinsed three times with G2 solvent and thoroughly dried in an argon-filled glove box to prevent contamination. For cathode-electrolyte interphase (CEI) analysis, NCM811 material was carefully scraped from the aluminum foil, ultrasonically dispersed in G2 solvent, and deposited onto a copper grid for transmission electron microscopy (TEM, FEI Tecnai F20) examination. To investigate the solvation structure and electrolyte composition, nuclear magnetic resonance (NMR, Bruker 400M) and Raman spectroscopy (alpha300 R, WITec) were employed. Additionally, in situ Raman spectroscopy (MAPS-Raman-532, Mekansm Technology) was utilized to analyze the evolution of the electric double layer structure near the positive electrode under varying applied voltages, providing real-time insights into the interfacial phenomena during electrochemical processes.

## 4.4 Calculation Methods

All electrolyte systems were investigated using classical molecular dynamics (MD) simulations implemented in Materials Studio. The simulation protocol consisted of the following steps: First, the initial configuration was generated using the Amorphous Cell module, where a cubic simulation box containing explicit solvent molecules and Li salts (with precise stoichiometric ratios provided in Table S2) was constructed. Subsequently, the system geometry was optimized using the Forcite module with the COMPASS III force field to achieve a stable initial configuration. The MD simulations were conducted in the NVT ensemble at 298 K for a production run of 50 ps, employing a time step of 1 fs. To model the electric double layer (EDL) formation under applied potentials, a system was constructed with two Pt(001) crystal planes serving as cathode and anode electrodes, separated by the electrolyte phase. A 10 nm vacuum layer was introduced between the electrolyte and periodic boundaries to eliminate artificial interactions. An external electric field was applied along the cathode-anode direction through custom script implementation. The system underwent geometry optimization prior to NVT ensemble dynamics simulations for EDL characterization.

## Appendix A. Supporting information

The Supporting Information is available online.

## References

[1] Z. Wen, W. Fang, L. Chen, Z. Guo, N. Zhang, X. Liu, G. Chen, Anticorrosive copper current collector passivated by self-assembled porous membrane for highly stable lithium metal batteries, Adv. Funct. Mater. 31 (2021) 2104930.

[2] Y. Gao, Q. Cao, J. Pu, X. Zhao, G. Fu, J. Chen, Y. Wang, C. Guan, Stable zn anodes with triple gradients, Adv. Mater. 35 (2023) 2207573.

[3] Z. Zhao, X. Zhao, Y. Zhou, S. Liu, G. Fang, S. Liang, Towards establishing uniform metrics for evaluating the safety of lithium metal batteries, Adv. Powder Mater. 2 (2023) 100139.

[4] G. Wu, Z. Weng, J. Li, Z. Zheng, Z. Wen, W. Fang, Y. Zhang, N. Zhang, G. Chen, X. Liu, Body armor-inspired double-wrapped binder with high energy dispersion for a stable $SiO_x$ anode, ACS Appl. Mater. Interfaces 15 (2023) 34852-34861.

[5] J. Pu, Q. Cao, Y. Gao, Q. Wang, Z. Geng, L. Cao, F. Bu, N. Yang, C. Guan, Liquid metal-based stable and stretchable Zn-ion battery for electronic textiles, Adv. Mater. 36 (2024) 2305812.

[6] S. Dai, W. Fang, T. Wang, Y. Gao, T. Zhang, Z. Qin, G. Chen, X. Zhou, Progresses on advanced electrolytes engineering for high-voltage lithium metal batteries, Chem. Eng. J. 500 (2024) 157269.

[7] Y. Gao, G. Wu, W. Fang, Z. Qin, T. Zhang, J. Yan, Y. Zhong, N. Zhang, G. Chen, Transesterification induced multifunctional additives enable high-performance lithium metal batteries, Angew. Chem. Int. Ed. 63 (2024) e202403668.

[8] Y. Wang, Y. Gao, J. He, J. Yang, G. Fu, Q. Cao, J. Pu, F. Bu, X. Xu, C. Guan, Sphere-Confined reversible zn deposition for stable alkaline aqueous batteries, Adv. Mater. 36 (2024) 2307819.

[9] Z. Wen, W. Fang, F. Wang, H. Kang, S. Zhao, S. Guo, G. Chen, Dual-Salt electrolyte additive enables

high moisture tolerance and favorable electric double layer for lithium metal battery, Angew. Chem. Int. Ed. 63 (2024) e202314876.

[10] J.B. Goodenough, Y. Kim, Challenges for rechargeable li batteries, Chem. Mater. 22 (2010) 587-603.

[11] P. Xiao, X. Yun, Y. Chen, X. Guo, P. Gao, G. Zhou, C. Zheng, Insights into the solvation chemistry in liquid electrolytes for lithium-based rechargeable batteries, Chem. Soc. Rev. 52 (2023) 5255-5316.

[12] Z. Qin, Y. Gao, F. Wang, W. Fang, T. Zhang, Y. Zhong, H. Liu, N. Zhang, X. Yuan, G. Chen, Dual-additive chemistry induced robust electrode-electrolyte interphases for high-performance lithium metal batteries, J. Power Sources 614 (2024) 235035.

[13] J.-G. Zhang, W. Xu, J. Xiao, X. Cao, J. Liu, Lithium metal anodes with nonaqueous electrolytes, Chem. Rev. 120 (2020) 13312-13348.

[14] Y. Zhong, X. Xie, Z. Zeng, B. Lu, G. Chen, J. Zhou, Triple-function hydrated eutectic electrolyte for enhanced aqueous zinc batteries, Angew. Chem. Int. Ed. 62 (2023) e202310577.

[15] Y. Gao, N. Yang, F. Bu, Q. Cao, J. Pu, Y. Wang, T. Meng, J. Chen, W. Zhao, C. Guan, Double-sided engineering for space-confined reversible Zn anodes, Energy Environ. Sci. 17 (2024) 1894-1903.

[16] Z. Wang, X. Che, D. Wang, Y. Wang, X. He, Y. Zhu, B. Zhang, Non-fluorinated ethers to mitigate electrode surface reactivity in high-voltage NCM811-Li batteries, Angew. Chem. Int. Ed. 63 (2024) e202404109.

[17] Z. Wen, W. Fang, X. Wu, Z. Qin, H. Kang, L. Chen, N. Zhang, X. Liu, G. Chen, High-concentration additive and triiodide/iodide redox couple stabilize lithium metal anode and rejuvenate the inactive lithium in carbonate-based electrolyte, Adv. Funct. Mater. 32 (2022) 2204768.

[18] X. Li, M. Li, Y. Liu, Y. Jie, W. Li, Y. Chen, F. Huang, Y. Zhang, T.M. Sohail, S. Wang, X. Zhu, T.

Cheng, M.D. Gu, S. Jiao, R. Cao, Fast interfacial defluorination kinetics enables stable cycling of low-temperature lithium metal batteries, J. Am. Chem. Soc. 146 (2024) 17023-17031.

[19] W. Fang, Z. Wen, F. Wang, L. Chen, Y. Zhang, N. Zhang, X. Liu, G. Chen, Triple-function eutectic solvent additive for high performance lithium metal batteries, Sci. Bull. 69 (2024) 1686-1696.

[20] W. Fang, Z. Wen, L. Chen, Z. Qin, J. Li, Z. Zheng, Z. Weng, G. Wu, N. Zhang, X. Liu, X. Yuan, G. Chen, Constructing inorganic-rich solid electrolyte interphase via abundant anionic solvation sheath in commercial carbonate electrolytes, Nano Energy 104 (2022) 107881.

[21] P. Liang, J. Li, Y. Dong, Z. Wang, G. Ding, K. Liu, L. Xue, F. Cheng, Modulating interfacial solvation via ion dipole interactions for low-temperature and high-voltage lithium batteries, Angew. Chem. Int. Ed. 64 (2024) e202415853.

[22] J. Xiang, Y.-C. Lu, Ether-based high-voltage lithium metal batteries: the road to commercialization, ACS Nano 18 (2024) 10726-10737.

[23] H. Wang, Z. Yu, X. Kong, S.C. Kim, D.T. Boyle, J. Qin, Z. Bao, Y. Cui, Liquid electrolyte: The nexus of practical lithium metal batteries, Joule 6 (2022) 588-616.

[24] M. Li, C. Chen, H. Luo, Q. Xu, K. Yan, Y. Qiu, G. Zhou, Constructing an inorganic-rich solid electrolyte interphase by adjusting electrolyte additives for stable Li metal anodes, J. Mater. Chem. A 12 (2024) 10072-10080.

[25] D. Zhao, L. Song, J. Wang, J. Zhang, X. Cui, P. Wang, J. Sun, X. Cai, J. Huang, N. Zhang, L. Zhang, S. Li, Insight into the competitive reaction between LiDFP and LiFSI in lithium-ion battery at low temperature, J. Power Sources 549 (2022) 232147.

[26] H. Zheng, H. Xiang, F. Jiang, Y. Liu, Y. Sun, X. Liang, Y. Feng, Y. Yu, Lithium difluorophosphate-

based dual-salt low concentration electrolytes for lithium metal batteries, Adv. Energy Mater. 10 (2020) 2001440.

[27] Y. Zhang, F. Li, Y. Cao, M. Yang, X. Han, Y. Ji, K. Chen, L. Liang, J. Sun, G. Hou, Tuning the FEC-related electrolyte solvation structures in ether solvents enables high-performance lithium metal anode, Adv. Funct. Mater. 34 (2024) 2315527.

[28] A. Dutta, K. Matsushita, Y. Kubo, Impact of glyme ether chain length on the interphasial stability of lithium-electrode in high-capacity lithium-metal battery, Adv. Sci. 11 (2024) 2404245.

[29] Q. Wu, M.T. McDowell, Y. Qi, Effect of the electric double layer (EDL) in multicomponent electrolyte reduction and solid electrolyte interphase (SEI) formation in lithium batteries, J. Am. Chem. Soc. 145 (2023) 2473-2484.

[30] P.-C. Li, Z.-Q. Zhang, Z.-W. Zhao, J.-Q. Li, Z.-X. Xu, H. Zhang, G. Li, Dipole moment influences the reversibility and corrosion of lithium metal anodes, Adv. Mater. 36 (2024) 2406359.

[31] Z. Wang, C. Chen, D. Wang, Y. Zhu, B. Zhang, Stabilizing interfaces in high-temperature NCM811-Li batteries via tuning terminal alkyl chains of ether solvents, Angew. Chem. Int. Ed. 62 (2023) e202303950.

[32] W. Zhang, Y. Lu, L. Wan, P. Zhou, Y. Xia, S. Yan, X. Chen, H. Zhou, H. Dong, K. Liu, Engineering a passivating electric double layer for high performance lithium metal batteries, Nat. Commun. 13 (2022) 2029.

[33] Z. Qin, T. Zhang, X. Gao, W. Luo, J. Han, B. Lu, J. Zhou, G. Chen, Self-reconstruction of highly degraded $LiNi_{0.8}Co_{0.1}Mn_{0.1}O_2$ toward stable single-crystalline cathode, Adv. Mater. 36 (2024) 2307091.

[34] P. Yuan, T. Zhang, Z. Qin, Y. Gao, X. Long, Z. Qin, N. Zhang, C. Jia, G. Chen, High temperature molten salts mediated deep regeneration and recrystallization of ternary nickle-rich cathodes, Adv. Powder Mater. 4 (2025) 100266.

[35] S.C. Kim, J. Wang, R. Xu, P. Zhang, Y. Chen, Z. Huang, Y. Yang, Z. Yu, S.T. Oyakhire, W. Zhang, L.C. Greenburg, M.S. Kim, D.T. Boyle, P. Sayavong, Y. Ye, J. Qin, Z. Bao, Y. Cui, High-entropy electrolytes for practical lithium metal batteries, Nature Energy 8 (2023) 814-826.

[36] J. Yan, J. Li, W. Fang, Y. Gao, Z. Qin, M. Sun, Y. Zhang, N. Zhang, X. Liu, G. Chen, Sustainable release of borate- and nitrate- electrolyte additives via metal-organic frameworks nanocapsules for stable lithium metal batteries, Chem. Eng. J. 494 (2024) 153104.

[37] Z. Qin, Y. Zhang, W. Luo, T. Zhang, T. Wang, L. Ni, H. Wang, N. Zhang, X. Liu, J. Zhou, G. Chen, A universal molten salt method for direct upcycling of spent Ni-rich cathode towards single-crystalline Li-rich cathode, Angew. Chem. Int. Ed. 62 (2023) e202218672.

[38] D. Chai, Y. Zhu, C. Guan, T. Zhang, S. Tang, H. Zhu, X. Li, Y. Fu, Achieving stable interphases toward lithium metal batteries by a dilute and anion-rich electrolyte, Energy Storage Mater. 62 (2023) 102957.

[39] Y. Yang, X. Wang, J. Zhu, L. Tan, N. Li, Y. Chen, L. Wang, Z. Liu, X. Yao, X. Wang, X. Ji, Y. Zhu, Dilute electrolytes with fluorine-free ether solvents for 4.5 V lithium metal batteries, Angew. Chem. Int. Ed. 63 (2024) e202409193.

[40] Z. Qin, Y. Gao, T. Zhang, Y. Li, R. Zhao, N. Zhang, X. Liu, L. Chen, G. Chen, Rapid desolvation and anti-reduction electrolyte enables high-performance lithium metal batteries, Energy Lab 2 (2024) 240012.

[41] X. Wang, Z. Li, Q. Mao, S. Wu, Y. Cheng, Y. Qin, Z. Chen, Z. Peng, X. Yao, D. Wang, Electrolyte-independent and sustained inorganic-rich layer with functional anion aggregates for stable lithium metal electrode, Adv. Powder Mater. 4 (2025) 100261.